Sensors and Actuators Reports 9 (2025) 100273

Contents lists available at ScienceDirect

Sensors and Actuators Reports

journal homepage: www.sciencedirect.com/journal/sensors-and-actuators-reports

Fast and sensitive virus detection using a plasmonic sensor that integrates electrokinetically assisted sampling and surface-enhanced Raman scattering

Shamim Azimi [a], Maryam Moridsadat [b], Bhavin Shastri [b], Bruce W. Banfield [c], Carlos Escobedo [a], Aristides Docoslis [a,*]

[a] QuSENS Laboratory, Department of Chemical Engineering, Queen's University, Kingston, ON K7L 3N6, Canada
[b] Centre for Nanophotonics, Engineering Physics & Astronomy, Queen's University, Kingston, ON K7L 3N6, Canada
[c] Department of Biomedical and Molecular Sciences, Queen's University, Kingston, ON K7L 3N6, Canada

ARTICLE INFO

Keywords:
Surface-enhanced Raman scattering (SERS)
Dielectrophoresis
Silver nanoparticle, label-free, virus detection

ABSTRACT

We present a novel plasmonic biosensing method for on-chip detection on viral particles featuring a microelectrode platform that integrates accelerated sampling of virus with surface-enhanced Raman scattering (SERS). We show experimentally that our approach can produce spectacular results owing to the unique incorporation of two key features: (1) Concentration amplification of virus on the SERS-active substrate; (2) Local plasmonic activity enhancement due to the targeted superimposition of silver nanoparticles on the captured virus sites. When tested for the detection of the M13 bacteriophage our "sandwich" assay yielded excellent reproducibility (signal variation <6 %) and a very low limit of detection (1.13×10^2 pfu/ml). Compared with the performance of our standard SERS substrates, SERS signals stronger by at least one order of magnitude are typically achieved. In addition to experimental results, our work also includes finite element (COMSOL Multiphysics) and finite-difference time-domain (FDTD) simulations that provide insights into the mechanisms of concentration amplification and plasmonic activity enhancement, respectively.

1. Introduction

Recent epidemics (e.g., Ebola virus disease, Zika virus), pandemics (e.g., SARS-CoV-2, H1N1) and the higher costs associated with their containment and treatment emphasize our urgent need for methods that offer early and efficient detection of viral infections [1,2]. Safeguarding public health and safety through early diagnoses requires the implementation of efficient and cost- effective (bio)chemical diagnostic methods, preferably at the point of need. Accurate testing for viruses, however, typically requires time-consuming and laborious procedures performed in properly equipped, centralized facilities [3]. This translates into delayed diagnoses, higher health care costs, loss of work productivity, and, occasionally, preventable fatalities. On the other hand, quick diagnostic methods (e.g., rapid COVID tests) often return positive results only when the patient is already at or past the acute phase of the disease, limiting their effectiveness. Techniques such as extraction [4], chemical modification [5], and microbubbles [6] have been explored to address these challenges, but they come with their own limitations.

One approach that holds great promise for overcoming the sampling problem, thus allowing plasmonic sensors to reach their full potential relies on the use of electric fields [7–9]. Trapping and manipulation of nanoscopic objects with electric fields is challenging, however, and requires properly designed and operated microelectrodes. The spatially non-uniform AC (alternating current) electric fields generated by these microelectrodes interact with particles and fluid and bring about forces that are collectively termed AC electrokinetic effects. Although the integration of one or more of these effects into microfluidic systems led to fast and sensitive detection of cells and bacteria, studies on the electrokinetic manipulation of viruses are scarce [10–16].

The combination of electrokinetic effects with SERS has already resulted in successful and highly effective applications for detecting proteins and low molecular weight analytes [17–19]. To reduce trapping voltage, researchers have tried to increase the effective surface area of the electrodes by using metallic nanostructures like nanorods, nanostars, nanopillars, and gold nanoshells [20–23]. Although effective,

* Corresponding author.
E-mail address: docoslis@queensu.ca (A. Docoslis).

https://doi.org/10.1016/j.snr.2024.100273
Received 5 September 2024; Received in revised form 28 November 2024; Accepted 16 December 2024
Available online 26 December 2024

these scaffolds are typically fabricated using relatively costly and time-consuming fabrication methods, which limit their accessibility. For instance, previous studies included the fabrication of 3D Ag nanorods through nanoimprint lithography for SERS detection [24], hollow silver antennas prepared via ion-beam milling on a polymeric substrate to enhance plasmonic properties [25], and silver nanostar arrays fabricated using electron beam lithography (EBL) on a single layer of graphene for detection purposes [26] Using the M13 virus as an illustrative example, we demonstrate an efficient experimental approach for achieving accelerated virus sampling and sensitive detection through the integration of electric field effects and SERS on a single microelectrode platform. Virus sampling, Ag nanoparticle capture, and SERS measurements are performed sequentially during an experimental procedure that we term LESS (an abbreviation for Label-free, Electric field-assisted, Sandwich-based, Surface-enhanced Raman scattering). The two key features of LESS are: (a) the use of AC electric field effects to overcome mass transfer limitations and amplify the concentration of the virus on the SERS-active substrate; (b) the use of a subsequent AC electric field for attracting and superimposing silver nanoparticles on the sites of captured virus, hence creating plasmonically active clusters of higher intensity and surface density. In addition to experimental observations, we also employ COMSOL Multiphysics™ simulations to explore the role of the electric field effects in the transport and capture of M13 and to gain insights on the forces, flow patterns, and heating effects that take place during M13 sampling. Moreover, we perform preliminary finite- difference time-domain (FDTD) simulations to get an understanding of the SERS signal enhancement that is observed when Ag nanoparticles are superimposed on the captured M13 virus.

2. Materials and methods

2.1. Materials

Silver nitrate (AgNO3), trisodium citrate (Na3C6H5O7), trichloro (1H,1H,2H,2H perfluorooctyl) silane, and tris buffered saline (TBS) were all purchased from Sigma Aldrich (Oakville, ON, Canada). Standard silver nanoparticles (50 nm) were purchased from Cytodiagnostics (Burlington, ON, Canada; see Supporting Info). M13 bacteriophage was purchased from Cedarlane (Burlington, ON, Canada). Polished silicon wafers (4″ diameter) with a thermally grown SiO2 layer (0.5 μm) were purchased from University Wafer (South Boston, MA, US). Millipore® water (18.2 MΩ cm) was used to prepare all aqueous solutions. A transparency-based photolithography mask was designed using AUTOCAD (2018) and printed by Advance Reproductions Corp. (North Andover, MA, US).

2.2. Microchip fabrication and modification

Microelectrodes were fabricated using a photolithography process on silicon wafers, followed by electron beam metal film evaporation and lift-off [27].

After undergoing a 5 min surface cleaning process through exposure to an oxygen plasma atmosphere, the microelectrode chips were rendered hydrophobic by being treated with trichloro(1H,1H,2H,2H-perfluorooctyl) silane. Specifically, a 20 μL droplet of the silane solution was placed on each chip and was allowed to react overnight in a low-vacuum environment. After the reaction was complete, the chips were thoroughly cleaned with acetone, ethanol, and water before being air-dried and stored for future use.

2.3. Assembly of dendritic nanostructures

The fabrication of the silver dendritic nanostructures followed the procedure outlined by Raveendran et al. [27]. In brief, a droplet containing a mixture of 2 mM Na3C6H5O7 and 0.5 mM AgNO3 was placed on the microelectrode chip. All the fabrication steps were conducted on a custom-made chip holder, which supported the microelectrode chips and facilitated their electrical connection to the function generator. The electrical signal was applied using a BK Precision 4040B Sweep function generator (Cole-Parmer Canada Inc.) while being monitored with a Tektronix 1002B oscilloscope. The applied voltage was 2.5 Vpp (peak-to-peak voltage) and the frequency was set to 10 Hz. For simplicity, the external AC potential was applied to only two adjacent microelectrodes each time. The voltage was applied for a duration of 10 min in all experiments. At each voltage cycle, silver ions were reduced (Eqn. 1) at the microelectrode that served as cathode, while citrate ions were oxidized (Eqn. 2) at the microelectrode that served as anode. These reactions led to the formation of dendritic nanostructures starting at the edges of the microelectrodes and growing over the insulating substrate. After the nanostructures were formed and the reagent solution was removed, the substrates were thoroughly rinsed with distilled water and 2 mM aqueous potassium iodide (SSKI oral solution) to eliminate any remaining citrate.

$$Ag^{+}_{(aq)} + e^{-} \rightarrow Ag_{(s)} \quad (1)$$

$$C_6H_5O_7^{3-}(Aq) \rightarrow CO_{2\ (aq)} + H^{+}_{(aq)} + C_5H_4O_5^{2-}(aq) + 2e^{-} \quad (2)$$

2.4. Preparation of virus

The M13 phage (ATCC# 15,669-B1) was acquired in a desiccated state from Cedarlane (Ontario). The phage was resuspended by mixing it with 1 mL of Yeast-Tryptone broth, composed of 3 L of water, 24 g of tryptone, 15 g of yeast extract, and 15 g of NaCl, with a pH of 7.5. The cultures were incubated at 37 °C with shaking at 230 rpm for 18 h. To culture the M13 phage, nutrient-deficient M9 plates were used to prepare E. coli EMG31. The M9 plates were made by combining 800 mL of water, 18 g of agar, 10 mL of 10 mM $CaCl_2$, 1 mL of 1 M $MgSO_4{\cdot}7H_2O$, 10 mL of 20 % glucose, 1 mL of 1 % Thiamine HCl, and 200 mL of M9 salt solution (made with 1 L of water, 5.0 g of NH_4Cl, 2.5 g of NaCl, 15 g of KH_2PO_3, and 64 g of $Na_2HPO_4{\cdot}7H_2O$). The E. coli EMG31 was then transferred to 26 mL of Yeast-Tryptone broth and grown until it reached the log growth phase. Following that, 200 μL of the log growth E. coli EMG31 was mixed with 10 μL of the resuspended M13 phage and added to 20 mL of Yeast-Tryptone broth. After 1.5 h, the solution was divided into centrifuge-safe sample holders, with each holder containing 2 mL of the solution. After an additional 6 h, the samples were centrifuged and decanted. The samples were found to have an approximate concentration of 10^{13} pfu/mL via plaque assay and were stored at 4 °C until required. The cultures were incubated at 37C while shaking at 230 rpm for 18 h.

2.5. Application of LESS

For virus sampling and concentration, 10 μL of the virus solution was carefully dispensed onto the microelectrode's center using a micropipette. To capture viral particles from buffer solution, an electric field with a frequency of 100 kHz and a voltage of 10 Vpp was applied for 8 min, followed by gentle drying with a nitrogen stream.

Next, to capture AgNPs onto the virus-containing dendrites, 10 μL of a AgNP dispersion (2.91×10^{13} particles/mL)) was added to the microelectrodes. Prior to use, the AgNPs were centrifuged twice at 6000 rpm for 30 min and washed with Millipore® water to remove the supernatant. The collection of AgNPs was then conducted for 8 min using an electric field at 10 kHz and 18 Vpp.

2.6. Characterization

Field emission scanning electron microscopy (FESEM) was performed using a ThermoFisher Quanta 650 FEG ESEM to visualize the formation of LESS. Fluorescent microscopy was carried out on Nikon Eclipse Ti2-LAPP inverted microscope.

2.7. Fluorescence microscopy

The microelectrodes were initially incubated with 50 µL of a blocking solution (3 % BSA in PBS) for 1 hour without shaking. Subsequently, they were rinsed with 5 mL of PBS for 5 min to remove any excess blocking buffer. Next, the M13 phage capture was performed by exposing the microelectrodes to 10 Vpp and 100 kHz, with a concentration of 10^9 pfu/ml. Subsequently, the microelectrodes underwent another gentle 5-minute rinse with 5 mL of PBS to eliminate any unbound M13 bacteriophage. In the following step, the microelectrodes were incubated with 2.5 mL of biotinylated anti-fd solution (diluted in PBS to a final concentration of 2 µg/mL) for 1 hour with gentle shaking. This process was followed by another gentle 5-minute rinse with 5 mL of PBS to remove any unbound biotinylated anti-fd. Afterward, the microelectrodes were exposed to 2.5 mL of streptavidin-FITC solution (diluted in PBS to a final concentration of 1 µg/mL) for 1 hour with gentle shaking. A final gentle 5-minute rinse with 5 mL of PBS was performed to remove any unbound streptavidin-FITC. Finally, the presence of M13 bacteriophage on the surface was detected by observing the microelectrodes under a fluorescence microscope, completing the detection process. Fluorescent and brightfield images of the virus were captured using an Olympus IX83 inverted epi-fluorescent microscope (Tokyo, Japan) equipped with a low-noise, high-speed CMOS camera (Zyla4.2-CL10, ANDOR, Belfast, Ireland).

2.8. Raman measurements

SERS spectra were acquired by using a HORIBA Jobin-Yvon Raman Spectrometer (Model LabRAM), equipped with a 632.8 nm He/Ne laser (17 mW), 1800 lmm^{-1} grating, and an Olympus BX-41 microscope system. The spectral collection was conducted in backscattered mode with $a \times 50$ microscope objective, using a 500 µm pinhole and a 500 µm slit width, with a sampling time of 10 s. Polynomial subtraction was applied for background correction, and the Savitsky–Golay filter was utilized to reduce noise. Data analysis and visualization were performed using Python programming language with the Pandas and Matplotlib libraries utilized for reading and plotting data, respectively [29]. Raman mapping was acquired using an XploRA™ PLUS Micro Raman Spectrometer (HORIBA France SAS) equipped with SWIFT™ confocal microscopy.

3. Results and discussion

3.1. AC electric field effects

Effective transfer of analytes to the SERS substrate is crucial to achieve sensitive and reproducible measurements. Typically, analytes are driven to the substrate by adsorption from solution or drop-casting (solvent drying), but both methods have their drawbacks. Adsorption has poor reproducibility and low analyte association, especially with dilute samples. Drop-casting can cause uneven deposition due to 'coffee ring' effects or capillary wicking. We attempt to overcome these issues with the use of AC electric field effects. Such fields can be conveniently applied in our case by making use of microelectrodes already embedded in the SERS chip, i.e., the ones previously used for the electrodeposition of the SERS-active silver substrate. The application of AC potential across the microelectrodes brings about a host of phenomena in the virus-containing liquid sample. The electric field generated phenomena that are being used in our case are: Dielectrophoresis (DEP), a deterministic particle motion resulting from the interaction between particles and a spatially non-uniform electric field by means of induced polarization effects; AC electroosmosis (ACEO), originating from the interaction of the tangential component of the electric field with the induced charges in the diffuse double layer on the electrode surface.

Fig. 1.

Electrothermal fluid flow (ETFF) is generated by the interaction of the field with an electrically inhomogeneous liquid due to local ohmic heating and resulting temperature gradients. The effect of these forces on a virus-containing sample situated on the SERS chip is schematically depicted in Fig. 2a, DEP is the result of a direct force ("dielectrophoretic force") on the virus and can cause its transport and capture onto the SERS-active layer. ACEO and/or ETFF act indirectly on the virus by means of a Stokes (drag) force as the fluid moves past the virus particles. ACEO and ETFF have a "conveyor" belt effect that can bring virus close

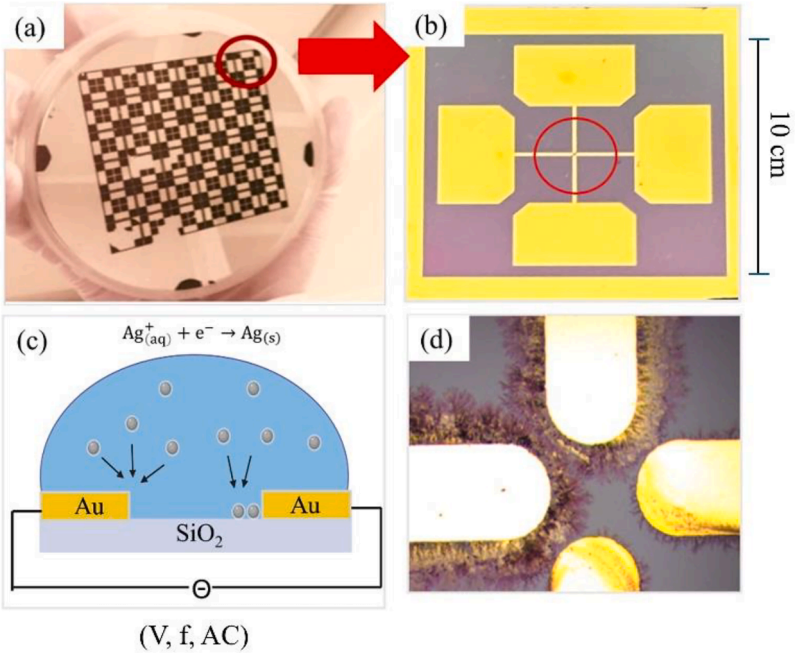

Fig. 1. (a) A batch of microelectrode chips fabricated using photolithography. (b) Top view of a single microelectrode chip. (c) Schematic depicting growth of Ag dendritic nanostructures between adjacent gold microelectrodes (cross sectional view) energized by an AC electric field. (d) Optical image of Ag dendritic nanostructures grown under 10 Hz, 3 Vpp.

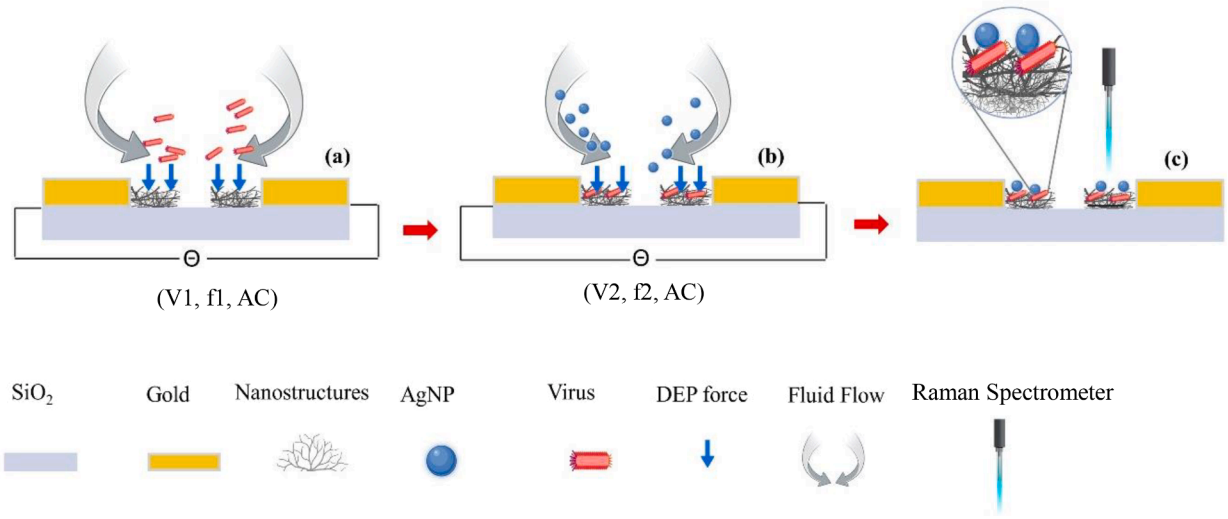

Fig. 2. Steps involved in LESS. (a) Accelerated transport and active capture of virus particles onto the substrate. (b) Formation of a sandwich structure by superimposing actively captured AgNPs on the virus. (c) SERS data acquisition.

to the SERS substrate from remote areas inside the sample and, thus, accelerate the sampling outcome. It is worth noting that ACEO is prevalent in aqueous media of low ionic strength, while ETFF becomes stronger as the ionic conductivity of the medium increases. Therefore, these two flows may occur simultaneously, or one at a time. Finally, it must be pointed out that all three aforementioned effects are strongly dependent on both amplitude and frequency of the applied electric field. This dependence constitutes a major advantage, as it permits us to finetune analyte sampling by varying simple experimental parameters.

In addition to providing effective sampling, LESS also takes advantage of electric fields to increase the intensity of the plasmonic effect of the SERS-active substrate. This is accomplished in a subsequent step when, following the removal of the virus sample, a suspension of Ag nanoparticles is deposited on the same SERS substrate (Fig. 2b). An electric field of different characteristics (voltage, frequency) is now applied on the suspension, resulting in nanoparticle transport and accumulation on the virus collection site. This effect is expected to create Ag nanoparticle clustering on or near the virus particles and, consequently, a higher density of SERS hot spots (Fig. 2c). Below we perform a series of experiments to validate our hypothesis.

3.2. Virus sampling

We employ fluorescence imaging to visually confirm the accumulation of viral particles on dendritic nanostructures when an electric field is applied across the microelectrodes. The results can be seen in Fig. 3. The dashed lines indicate the position of the microelectrodes on the SERS layer. Fig. 3a shows the fluorescence image acquired in the case of virus sampling occurring by means of diffusion. In this case, no accumulation of virus can be seen. Fig. 3b is the corresponding brightfield image (Fig. 3b), which shows clearly the SERS layer that has formed around the two electrodes (top and left) that were activated during the Ag electrodeposition process. In contrast, Fig. 3c shows a much stronger fluorescence signal and the formation of bright streaks on the SERS layer, which follows the outline of the microelectrode boundaries. This image corresponds to virus sampling with the aid of an AC signal applied across two adjacent microelectrodes. The intense fluorescence indicates a virus accumulation pattern that is consistent with the theory of DEP,

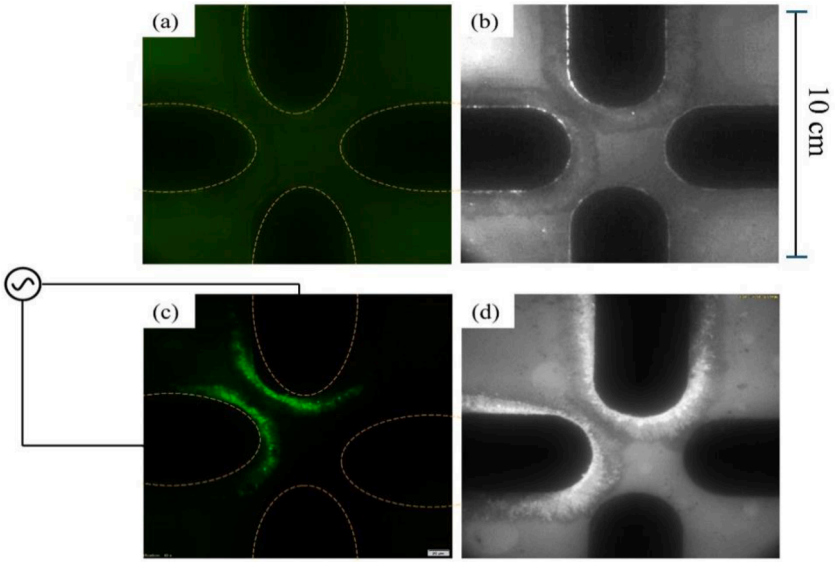

Fig. 3. (a) Fluorescence imaging and (b) brightfield image showing the deposition of viral particles on nanostructures without AC electric field. (c) Fluorescence imaging and (d) brightfield image showing the deposition of viral particles on nanostructures with AC electric field.

which calls for high accumulation in areas of narrow microelectrode gap. The strongest force occurs in areas where the intensity of the electric field gradient is the highest. The dendritic Ag nanostructures, which are physically connected to the microelectrodes decrease the microelectrode gap and, consequently, increase further the local electric field intensity ($E = V/d$). Hence, viral particles experience a stronger DEP force in these regions, which results in higher accumulation. The corresponding brightfield image is given in Fig. 3d.

3.3. Ag nanoparticle superimposition

In addition to achieving concentration amplification on the SERS-active surface, electric field effects can also be employed for the clustering of Ag nanoparticles on the locations of captured virus. It is expected that the combination of the two effects will further boost the SERS signal produced by the virus. The role of the SERS-active layer in the active capture of virus and Ag nanoparticles can be better understood upon inspection of its morphology. The FESEM image shown in Fig. 4 provides detailed information on the shape and architecture of the SERS-active layer (Fig. 4a). Specifically, the electrodeposited Ag nanostructures have a branched ("dendritic") morphology and extend for approximately 100 μm into the microelectrode gap. The length of the branched layer can be controlled by adjusting the distance between opposite microelectrodes [28]. Although these dendrites grow outwards from opposite microelectrodes, they never contact each other. We have recently shown that the electrical sorting of the structures is prevented due to the high-pressure gradients that develop as the dendrites from opposite electrodes reach a separation of a few micrometers [29]. This self-terminated growth of the dendrites ensures that an electric field will be present every time an electric potential difference is applied across the electrodes. Moreover, the intense topography of the Ag nanostructures produces asperities (tips, edges, etc.) that can amplify the local intensity of the electric field gradients. The latter gives rise to strong dielectrophoretic forces that attract and capture particles (virus and metallic nanoparticles) from the suspension. Evidence of that is provided in Fig. 4b, which shows the accumulation of Ag nanoparticles (bright clusters) on the surface of the dendrites. The nanoparticles were collected from a droplet (2.91×10^{12} particles/mL) that was deposited on the SERS chip for 10 min when a signal of 10Vpp and 100 kHz was applied across the microelectrodes. As can be seen from the FESEM images of Fig. 2b–d, the density of Ag nanoparticles captured on the surface correlates positively with the volumetric concentration of AgNP in the droplet. Notably, when the AgNPs suspension is concentrated 10-fold (2.91×10^{13} nanoparticles/mL), the SERS substrate appears to be densely covered by AgNPs over a large coverage area (Fig. 2d). Hence, it is expected that the high-density of AgNPs will create numerous additional hot spots and, in turn, stronger SERS signals. This hypothesis is put to test in the following section for the case of virus detection.

3.4. SERS-based detection using LESS

To demonstrate the sensitivity and reproducibility of LESS in pathogen sensing, we employed the M13 bacteriophage as our model analyte. This filamentous virus is known for its ability to infect Escherichia coli. It serves as a valuable tool in various scientific fields, including DNA replication, gene expression, protein synthesis, biotechnology, and recombinant protein production, as well as in introducing foreign DNA into host cells [30]. Fig. 5 is a schematic representation of a M13 phage which outlines the various proteins on the surface [31]. Major peak assignments in the SERS spectrum of M13 are shown in Table of Fig. 5.

To explore potential benefits from the use of LESS, the method was compared against simpler virus sampling methods, namely, colloidal interactions and drop casting. The comparison also included "active" sampling of virus (use of an AC electric field). In all cases, the SERS chips were produced under identical conditions and the virus concentration in the sample (TBS buffer) was kept constant and equal to 10^7 pfu/ml. The SERS signals obtained in each case can be seen in Fig. 6. Sampling by colloidal interactions produced a very weak signal, even at this relatively high virus concentration. This weak signal is likely due to the low

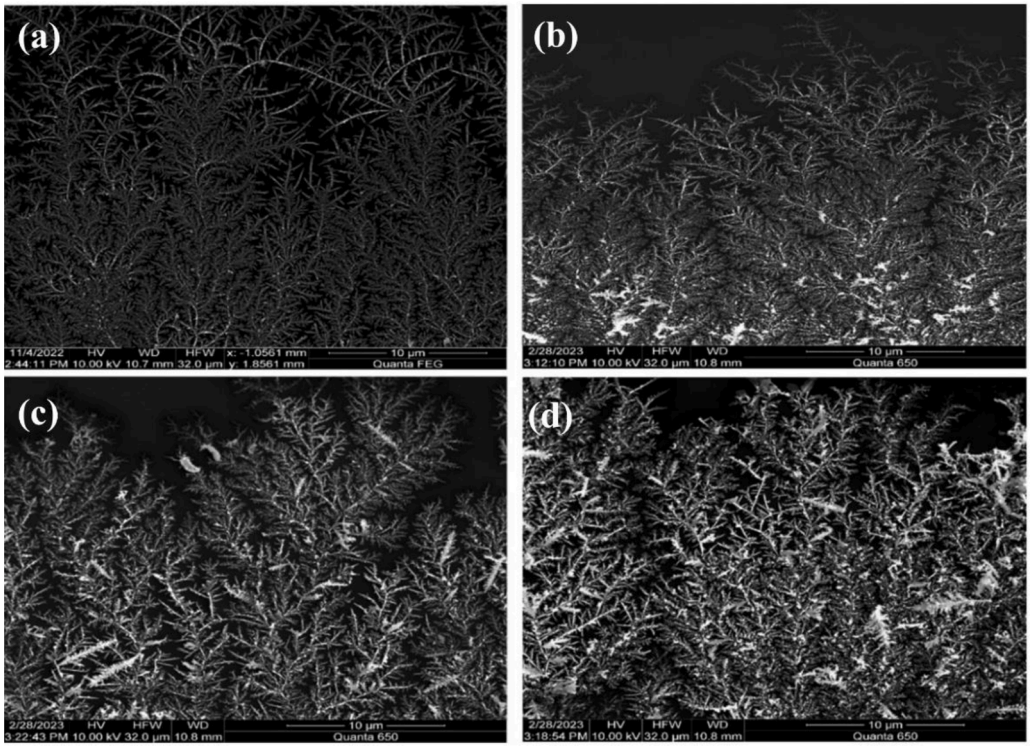

Fig. 4. FESEM images of silver nanostructures: a) without AgNPs, b) with AgNPs (original concentration), c) with AgNPs (5-fold concentration), and d) with AgNPs (10- fold concentration).

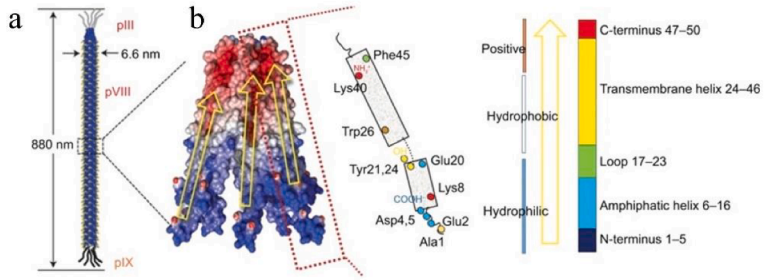

Peak wavenumber (cm^{-1})	Peak Assignment	Peak wavenumber (cm^{-1})	Peak Assignment
742	Adenine ring	1368	$V(COO^-)$
839	Tyr	1428	$-CH_2$ deformation mode
919	-COO stretch	1483	$-CH_2$ deformation mode
1024	Phe	1537	Trp
1183	$-CH_2$ bending mode	1586	$V(COO^-)$
1224	Amide III	1621	Amide I

Fig. 5. (a) Shape and dimensions of M13 bacteriophage and (b) Tertiary structure of envelope proteins [45]. Table listing main Raman peak assignments [32–37].

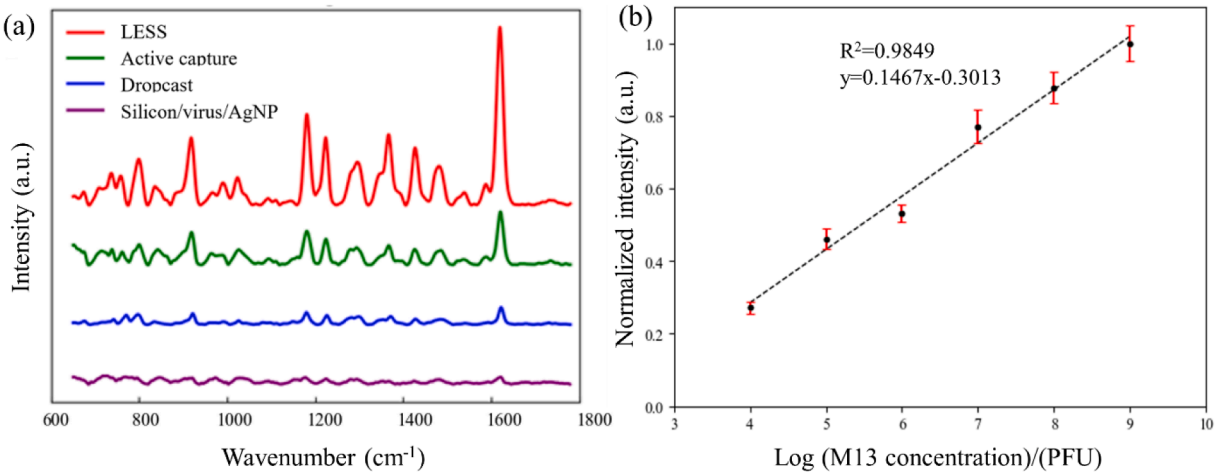

Fig. 6. (a) SERS spectra of M13 (10^7 pfu/ml) collected on the substrate through adsorption, dropcasting, active capture, and LESS. (b) Normalized SERS signal intensity variation of virus in buffer solution corresponding to the characteristic signal at 1183 cm^{-1}.

sensitivity of the assay, resulting from the limited interaction between the virus and the substrate, as well as the slow, diffusion-control transport of the target. The method of drop casting, which effectively deposits on the SERS chip all the virus contained in the droplet, produced a relatively stronger signal. On the other hand, "active" virus capture resulted in much stronger signal intensity, on account of the targeted virus deposition on the SERS-active surface. Finally, a substantial SERS signal enhancement was seen when LESS was employed. The sharper and stronger SERS signal seen in the latter case should be attributed to the deposition of silver nanoparticles (AgNPs) over the captured virus. The "sandwich" configuration that is created by enclosing the virus inside two layers of SERS-active silver results in a significantly stronger plasmonic effect. In this test, LESS produced a signal that was 14-fold stronger than that obtained from drop casting the virus sample on the SERS substrate.

LESS was tested further by employing samples of different virus loading (for SERS spectra, see Supporting Information). By using the peak at 1183 cm^{-1}, a clear correlation (R^2=0.9849) was found between virus concentration and signal intensity. Using the calibration curve shown in Fig. 6b, a limit of detection of 1.13×10^2 pfu/ml was calculated (The details of the calculation can be found in the Supporting Information). The assay allows us to detect several weaker characteristic M13 bands in the SERS spectra at concentrations as low as 1×10^4 pfu/ml. According to information found in the literature, these bands are attributed to the C—C twisting mode of the tyrosine residues (742 cm^{-1}), C—C stretching mode (839 cm^{-1}), -COO stretch (919 cm^{-1}), CH_2 bending mode (1183 cm^{-1}), $-CH_2$ bending mode at 1428 cm^{-1}, and Amide I at 1625 cm^{-1}, associated with the C = O stretching mode of the peptide backbone, respectively [32,38–41]. The SERS spectra of M13 over the range of 10^4–10^9 pfu/ml can be seen in the Supporting Information. Our SERS detection platform addresses a relatively unexplored area, since only one other study has focused on the SERS detection of M13

bacteriophage [42] (see also Figure S3). While that study reported weaker signals, our approach demonstrates a significant improvement in SERS signal quality. By combining electrokinetic sample collection with a sandwich assay, we achieve concentration amplification of the analyte and stronger signal intensities, thus significantly improving the overall effectiveness of viral detection with SERS.

The spatial variation of the SERS signal over the dendritic layer was assessed by means of confocal mapping and point-by-point measurements. Fig. 7 provides information on the SERS signal intensity of M13 (10^7 pfu/ml) as a function of position across an area of 400 μm^2 (box in Fig. 7a). The color map of Fig. 7c tracks the intensity of the peak at 1183 cm^{-1}. The result indicates relative uniformity of the SERS signal across the selected area. Fig. 7d shows SERS spectra collected from 20 random spots along the same substrate. The relative standard deviation (RSD) of the SERS peak intensities at 1183 cm^{-1} was <6 % (Fig. 7e), suggesting an overall consistent signal distribution.

3.5. Numerical investigation of electric field effects

3.5.1. COMSOL simulations

In this study, 2D COMSOL simulations were conducted in an effort to understand the type of electric field effects that take place during virus sampling inside a liquid medium and their role in the observed virus capture on the SERS-active surface. Key simulation results (Fig. 8) are shown for a plane normal to the substrate, drawn along the line of minimum separation (~42 μm) between adjacent microelectrodes. For viral particle capture, an applied AC signal of 10 Vpp at 100 kHz was used in the simulations.

Although the temperature rise observed in the system is modest—approximately 2 °C (Fig. 8a)—it is sufficient to generate strong fluid motion through ETFF (Fig. 8b). The enhanced ETFF acts as a "conveyor belt" that transports viral particles closer to the dendritic surface at speeds as high as 90 μm/s. In addition to ETFF, the simulation results show that the DEP force acting on the virus also plays a significant role. The time-averaged DEP force exerted on a spherical particle with radius "R" in a solution with dielectric permittivity of "ε_m" is given by:

$$F_{DEP}(\omega) = \pi\varepsilon_m R^3 \cdot \mathscr{R}e[K(\omega)]\nabla|E_{rms}|^2 \quad (3)$$

The direction of the dielectrophoretic force is determined by the sign of the *Re*[K(ω)] (=+0.636) and relies on the electrical conductivities and dielectric permittivities of the solution and particles. Under the conditions of our experiments, the viral particles experience positive DEP, i.e., they are attracted to locations that generate strong electric field gradients (electrode tips). The magnitude of the DEP force is proportional to the gradient of the electric field intensity squared, $\nabla|E_{rms}|^2$, where *Erms* represents the root mean square value of the electric field. The hydrodynamic diameter of the M13 was considered to be 6 nm [43]. The dielectrophoretic response of the virus was simulated using COMSOL in the AC/DC modules (Figs. 8c). As expected, the DEP force is the strongest in the area of SERS-active dendrites, since the electric field gradient is the highest at these locations (narrowest electrode gap).

In the presence of dendritic nanostructures, the logarithm of the force ratio (F_{DEP}/F_{drag}) varies between 10^6–10^8 in areas close to the electrodes and reaches a maximum value of 14 (fluid stagnation areas). This signifies the prevalence of the DEP force, resulting in enhanced trapping and concentration of viral particles at the electrode surface, as illustrated in Fig. 8d. Virus transport from distant locations, as well as stable trapping at the electrode surface, is therefore accomplished by combining these two mechanisms. The results indicate that the collection of M13 phage at the tips of microelectrodes can be achieved under the experimental conditions used in this study. Moreover, this collection pattern of the virus agrees with the theoretically expected virus collection pattern, as illustrated in our earlier research [44].

3.5.2. FDTD simulations

The SERS activity of a substrate relies on the enhancement of the local electric field near nanostructures. To further understand the observed increases in SERS performance when LESS is used, we conducted a series of simulations using commercial Lumerical software to solve Maxwell's equations and simulate the propagation of terahertz waves throughout the structure (Fig. 9). The finite-difference time-

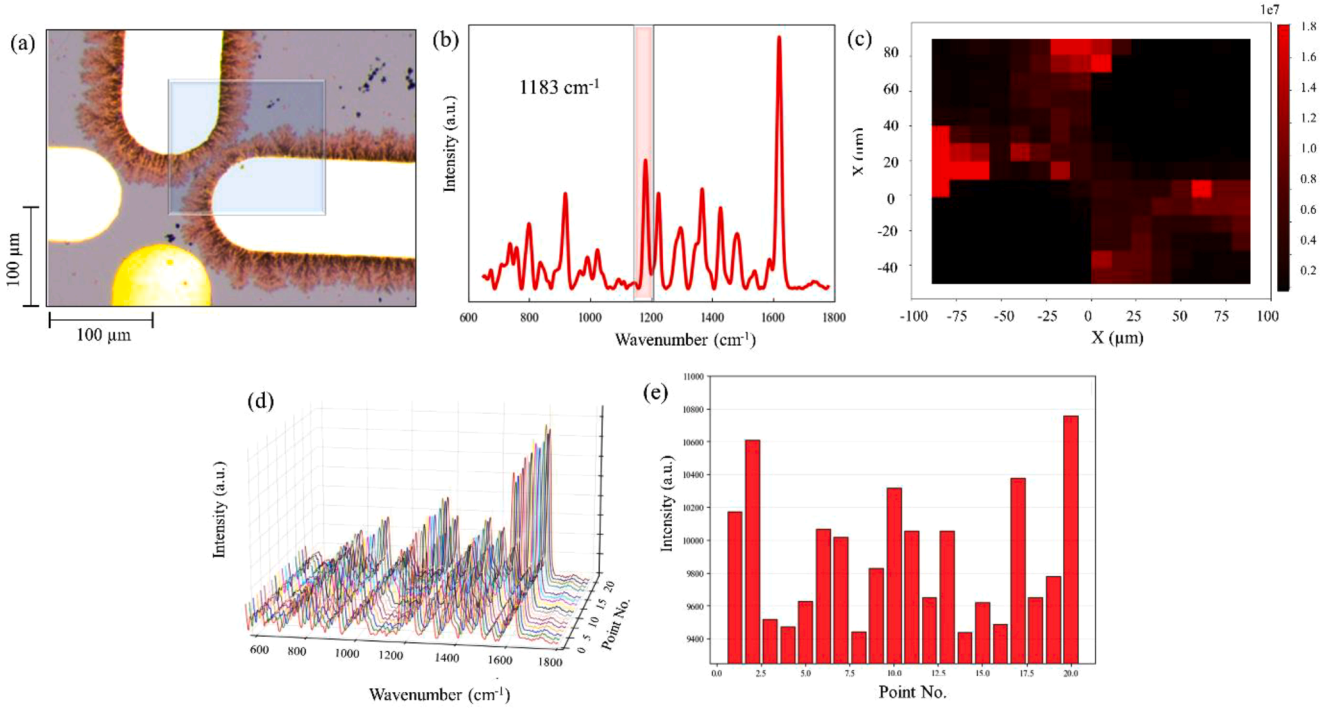

Fig. 7. (a) Optical image of the substrate (b) A respective SERS spectrum of 10^7 pfu/ml M13. c) Raman map of m13 by targeting the Raman shift at 1183 cm^{-1}. d) SERS spectra of 10^7 pfu/ml collected from 20 different spots on the same substrate. (e) Corresponding signal intensity distribution at 1183 cm^{-1}.

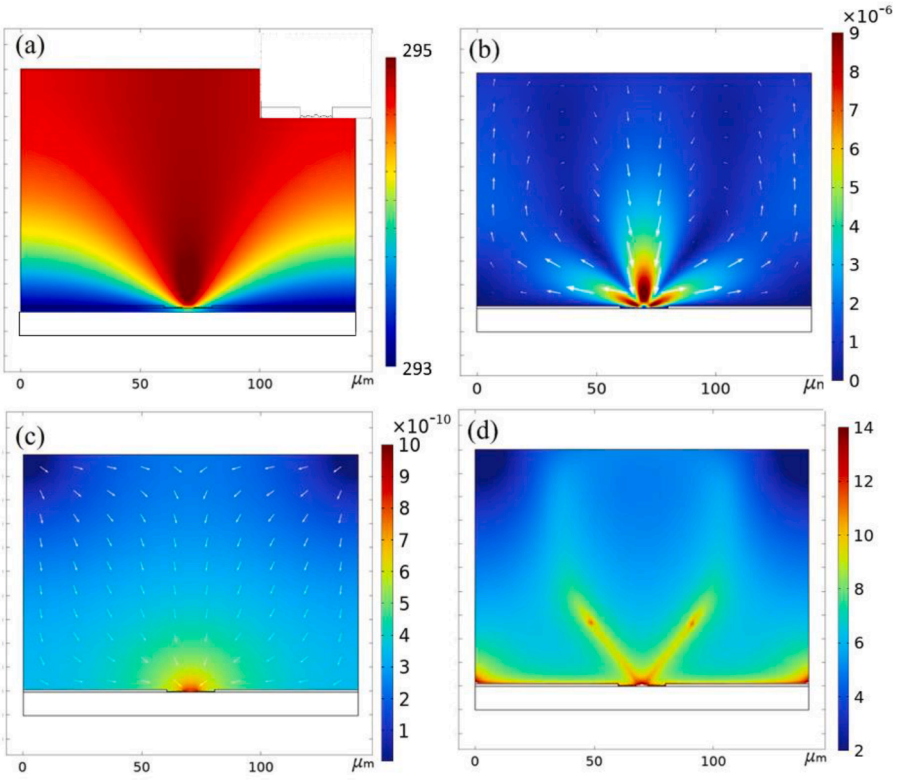

Fig. 8. (a) Cross-sectional view of the temperature profile (K) in the vicinity of the microelectrodes (inset). (b) Cross- sectional view of the fluid velocity (m/s). (c) Cross- sectional profile of the dielectrophoretic force. (d) Plot of log10($|F_{DEP}| / |F_{drag}|$) comparing the forces exerted on a virus particle (dielectrophoretic vs. viscous drag force).

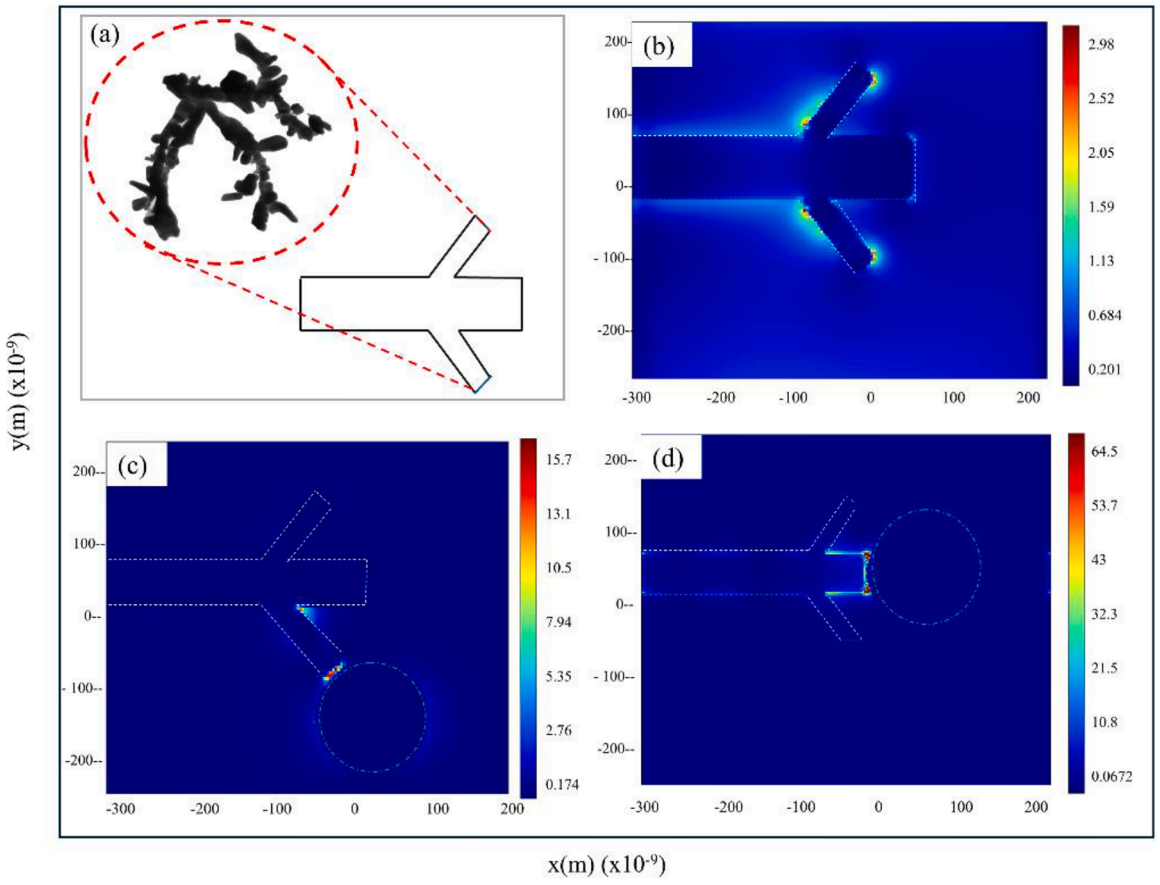

Fig. 9. FDTD simulations of the electromagnetic field around a typical Ag dendrite.

domain (FDTD) method was employed to calculate the electric and magnetic fields across different spatial points and wavelengths. The simulations were conducted for a 633 nm incident beam of light with vertical incidence, ensuring accurate representation of light interaction with the nanostructures on the substrate.

The enhancement factors (EF) observed in our FDTD simulations are referenced to a baseline EF value of 1.0, which represents the SERS signal intensity without any additional enhancement mechanisms. In Figs. 9c and 9d, the nanoparticles are positioned 5 nm away from the branches, to represent the case of a virus particle (5 nm in diameter) "sandwiched" between the branch and a silver nanoparticle. The color bars in Figs. 9b, 9c, and 9d demonstrate the spatial variation in EF across the SERS-active surface relative to this baseline.

Fig. 9a shows a TEM image of the SERS-active dendritic nanostructures. Fig. 9b exhibits the electric field enhancement of the bare dendrites (i.e., the nanostructure before silver nanosphere deposition), showing a low electric field enhancement of 2.98. To further study the assay, we explored different configurations of silver nanoparticles positioned on dendritic nanostructures. As shown in Figures 9c and 9d, these configurations demonstrate 15.7-fold and 64.5-fold electric field enhancements, respectively, due to the high electric field confinement between the silver branches and nanospheres. This shows the potential of nanoparticles to significantly enhance SERS signals by creating localized plasmonic hotspots, where the electric field is intensified.

By comparing our simulated EF values with experimental results for virus detection in the presence of nanoparticles, we find good agreement. This consistency reinforces our belief that the FDTD simulations can provide insights into the mechanisms that cause the observed SERS signal enhancement when LESS is applied.

4. Conclusions

Our study presents a novel SERS-based sensing method that leverages microscale electric fields for sensitive and label-free viral particle detection in liquid media. Starting with an already sensitive SERS substrate, we demonstrate an approach—termed LESS—that enhances its detection performance (by 14-fold) through the integration of accelerated virus sampling and silver nanoparticle superimposition. LESS showed high sensitivity and reproducibility in detecting the M13 virus, with a detection limit of 1.13×10^2 pfu/ml.

Additionally, our simulation results clarify mechanisms responsible for the enhanced detection performance observed. Specifically, COMSOL simulations illustrate how accelerated analyte transport and concentration amplification on SERS-active substrates can be achieved, while FDTD analysis revealed that enhanced plasmonic activity can result from the superimposition of silver nanoparticles on the captured virus. Our research demonstrates the strong potential for high-performance SERS sensing using metallic nanostructures and electric fields. It also lays the foundation for developing SERS-based sample analyses capable of providing rapid, sensitive, and label-free detection of viral particles in surface-based plasmonic biosensors.

CRediT authorship contribution statement

Shamim Azimi: Writing – review & editing, Writing – original draft, Software, Methodology, Investigation, Data curation. **Maryam Moridsadat:** Software, Data curation. **Bhavin Shastri:** Software, Data curation. **Bruce W. Banfield:** Supervision, Resources, Methodology, Conceptualization. **Carlos Escobedo:** Supervision, Software. **Aristides Docoslis:** Writing – review & editing, Supervision, Methodology, Investigation, Data curation, Conceptualization.

Declaration of competing interest

The authors declare that they have no known competing financial interests or personal relationships that could have appeared to influence the work reported in this paper.

Acknowledgments

Funding for this project was provided by the Government of Canada—Natural Sciences and Engineering Research Council of Canada (NSERC) Discovery Grants program and Mitacs Accelerate (in partnership with Spectra Plasmonics) to A.D. C. E. gratefully acknowledges financial support from NSERC, No. RGPIN-201–05138 and Canada Foundation for Innovation (CFI), No. 31967. The authors also thank Ms. A. Dobosz for her aid with SEM, and Dr. G. Gibson (Nanofabrication Kingston) for his aid in fabricating the microelectrode chips.

Supplementary materials

Supplementary material associated with this article can be found, in the online version, at doi:10.1016/j.snr.2024.100273.

Data availability

Data will be made available on request.

References

[1] N. McGarvey, M. Gitlin, E. Fadli, K.C. Chung, Increased healthcare costs by later stage cancer diagnosis, BMC. Health Serv. Res. (2022) 22, https://doi.org/10.1186/s12913-022-08457-6.
[2] K. Elsink, J.M. van Montfrans, M.E. van Gijn, M. Blom, P.M. van Hagen, T. W. Kuijpers, G.W.J. Frederix, Cost and impact of early diagnosis in primary immunodeficiency disease: a literature review, Clin. Immun. (2020) 213.
[3] A.M. Indelicato, Z.H. Mohamed, M.J. Dewan, C.P. Morley, Rapid antigen test sensitivity for asymptomatic COVID-19 screening, PRiMER. (2022) 6, https://doi.org/10.22454/primer.2022.276354.
[4] C. Liu, N. Yin, T. Jiang, Z. Li, C. Zhang, B. Man, J. Yu, Microextraction of electric fields and analytes by Janus hydrophobic/hydrophilic microfiber filter: application in Raman detection of persistent organic pollutants in complex liquid environments, Sensors Actuators Bl 397 (2023) 134709.
[5] A. Rahmani, A. Mohammadi, H.R. Kalhor, A continuous flow microfluidic device based on contactless dielectrophoresis for bioparticles enrichment, Electrophoresis 39 (2018) 445–455, https://doi.org/10.1002/elps.201700166.
[6] N. Ohannesian, J. Li, I. Misbah, F. Zhao, W.C. Shih, Directed concentrating of micro-/nanoparticles via near-infrared laser generated plasmonic microbubbles, ACS. Omega 5 (2020) 32481–32489, https://doi.org/10.1021/acsomega.0c04610.
[7] Cetin, B. Simulation of electrokinetic manipulation of particle motion inside microchannels. 2011, doi:10.13140/2.1.2362.6882.
[8] J. Wu, Y. Ben, D. Battigelli, H.C. Chang, Long-range AC electroosmotic trapping and detection of bioparticles, Ind. Eng. Chem. Res. 44 (2005) 2815–2822, https://doi.org/10.1021/ie049417u.
[9] D.S. Liao, J. Raveendran, S. Golchi, A. Docoslis, Fast and sensitive detection of bacteria from a water droplet by means of electric field effects and micro-raman spectroscopy, Sens. Biosensing. Res. 6 (2015) 59–66, https://doi.org/10.1016/j.sbsr.2015.09.005.
[10] D. Mantri, L. Wymenga, J. van Turnhout, H. van Zeijl, G. Zhang, Manipulation, sampling and inactivation of the SARS-COV-2 virus using nonuniform electric fields on micro-fabricated platforms: a review, Micromachines. (Basel) (2023) 14.
[11] A. Docoslis, L.A.T. Espinoza, B. Zhang, L.L. Cheng, B.A. Israel, P. Alexandridis, N. L. Abbott, Using nonuniform electric fields to accelerate the transport of viruses to surfaces from media of physiological ionic strength, Langmuir. 23 (2007) 3840–3848, https://doi.org/10.1021/la061486l.
[12] S. Stanke, C. Wenger, F.F. Bier, R. Hölzel, AC Electrokinetic Immobilization of Influenza Virus, Electrophoresis 43 (2022) 1309–1321, https://doi.org/10.1002/elps.202100324.
[13] M. Tomkins, D. Liao, A. Docoslis, Accelerated detection of viral particles by combining AC electric field effects and micro-raman spectroscopy, Sensors 15 (2015) 1047–1059, https://doi.org/10.3390/s150101047.
[14] M. Park, Surface display technology for biosensor applications: a review, Sensors (Switzerland) (2020) 20, https://doi.org/10.3390/s20102775.
[15] D. Akin, H. Li, R. Bashir, Real-time virus trapping and fluorescent imaging in microfluidic devices, Nano Lett. 4 (2004) 257–259, https://doi.org/10.1021/nl034987p.
[16] T. Schnelle, T. Moiler, S. Fiedler, S.G. Shirley, K. Ludwig, A. Herrmann, G. Fuhr, B. Wagner, U. Zimmermann, KURZE @ I z I-HMITTEILU NGEN trapping of viruses in high-frequency electric field cages, Springer-Verlag, 1996, p. 83.
[17] H. Dies, J. Raveendran, C. Escobedo, A. Docoslis, In situ assembly of active surface-enhanced raman scattering substrates via electric field-guided growth of dendritic nanoparticle structures, Nanoscale 9 (2017) 7847–7857, https://doi.org/10.1039/c7nr01743j.
[18] H. Dies, J. Raveendran, C. Escobedo, A. Docoslis, Rapid identification and quantification of illicit drugs on nanodendritic surface-enhanced raman scattering substrates, Sens. Actuators. B Chem. 257 (2018) 382–388, https://doi.org/10.1016/j.snb.2017.10.181.
[19] E.M. Laux, F.F. Bier, R. Hölzel, Electrode-Based AC electrokinetics of proteins: a mini-review, Bioelectrochemistry. 120 (2018) 76–82.
[20] Y. Gao, H. Zhu, X. Wang, R. Shen, X. Zhou, X. Zhao, Z. Li, C. Zhang, F. Lei, J. Yu, Promising mass-productive 4-inch commercial SERS sensor with particle in micro-nano porous Ag/Si/Ag structure using in auxiliary diagnosis of early lung cancer, Small. 19 (25) (2023) 2207324.
[21] I.B. Becerril-Castro, I. Calderon, N. Pazos-Perez, L. Guerrini, F. Schulz, N. Feliu, I. Chakraborty, V. Giannini, W.J. Parak, R.A. Alvarez-Puebla, Gold nanostars: synthesis, optical and SERS analytical properties, Anal. Sens. (2022) 2, https://doi.org/10.1002/anse.202200005.
[22] G. Fu, D.W. Sun, H. Pu, Q. Wei, Fabrication of gold nanorods for SERS detection of thiabendazole in apple, Talanta 195 (2019) 841–849, https://doi.org/10.1016/j.talanta.2018.11.114.
[23] Y. Gao, Y. Li, Y. Wang, Y. Chen, J. Gu, W. Zhao, J. Ding, J. Shi, Controlled synthesis of multilayered gold nanoshells for enhanced photothermal therapy and SERS detection, Small. 11 (2015) 77–83, https://doi.org/10.1002/smll.201402149.
[24] A. Colniță, D. Marconi, N.E. Dina, I. Brezeștean, D. Bogdan, I. Turcu, 3D silver metallized nanotrenches fabricated by nanoimprint lithography as flexible SERS detection platform, Spectrochim. Acta a Mol. Biomol. Spectrosc. (2022) 276, https://doi.org/10.1016/j.saa.2022.121232.
[25] G.C. Messina, M. Malerba, P. Zilio, E. Miele, M. Dipalo, L. Ferrara, F. de Angelis, Hollow plasmonic antennas for broadband SERS spectroscopy, Beilstein. J. Nanotechnol. 6 (2015) 492–498, https://doi.org/10.3762/bjnano.6.50.
[26] Y. Zhao, X. Li, Y. Liu, L. Zhang, F. Wang, Y. Lu, High performance surface-enhanced raman scattering sensing based on au nanoparticle-monolayer graphene-ag nanostar array hybrid system, Sens. Actuators. B Chem. 247 (2017) 850–857, https://doi.org/10.1016/j.snb.2017.03.063.
[27] J. Raveendran, K.G. Stamplecoskie, A. Docoslis, Tunable fractal nanostructures for surface-enhanced raman scattering via templated electrodeposition of silver on low- energy surfaces, ACS. Appl. Nano Mater. 3 (2021) 2665–2679, https://doi.org/10.1021/acsanm.0c00040.
[28] J. Raveendran, A. Docoslis, Portable surface-enhanced raman scattering analysis performed with microelectrode-templated silver nanodendrites, Analyst (2020), https://doi.org/10.1039/D0AN00484G.
[29] C. Vargas, F. Méndez, A. Docoslis, C. Escobedo, Theoretical analysis of dendrite formation generated in an electroosmotic flow with variable shape microelectrodes, Physics of Fluids (2024) 36, https://doi.org/10.1063/5.0188631.
[30] E. Stone, K. Campbell, I. Grant, O. McAuliffe, Understanding and exploiting phage–host interactions, Viruses. (2019) 11.
[31] W.J. Chung, D.Y. Lee, S.Y. Yoo, Chemical modulation of M13 bacteriophage and its functional opportunities for nanomedicine, Int. J. Nanomed. 9 (2014) 5825–5836, https://doi.org/10.2147/IJN.S73883.
[32] S. Shanmukh, L. Jones, J. Driskell, Y. Zhao, R. Dluhy, R.A. Tripp, Rapid and sensitive detection of respiratory virus molecular signatures using a silver nanorod array SERS substrate, Nano Lett. 6 (2006) 2630–2636, https://doi.org/10.1021/nl061666f.
[33] J. Sitjar, J.Der Liao, H. Lee, H.P. Tsai, J.R. Wang, P.Y Liu, Challenges of SERS technology as a non-nucleic acid or -antigen detection method for SARS-CoV-2 virus and its variants, Biosens. Bioelectron. 181 (2021) 113153, https://doi.org/10.1016/j.bios.2021.113153.
[34] P. Negri, Z.D. Schultz, Online SERS detection of the 20 proteinogenic L-amino acids separated by capillary zone electrophoresis, Analyst 139 (2014) 5989–5998, https://doi.org/10.1039/c4an01177e.
[35] A. Zengin, U. Tamer, T. Caykara, SERS detection of hepatitis B virus DNA in a temperature-responsive sandwich-hybridization assay, J. Raman Spectrosc. 48 (2017) 668–672, https://doi.org/10.1002/jrs.5109.
[36] Y. Tzeng, B.Y. Lin, Silver SERS adenine sensors with a very low detection limit, Biosensors. (Basel) (2020) 10, https://doi.org/10.3390/BIOS10050053.
[37] F. Inci, O. Tokel, S. Wang, U.A. Gurkan, S. Tasoglu, D.R. Kuritzkes, U. Demirci, Nanoplasmonic quantitative detection of intact viruses from unprocessed whole blood, ACS. Nano 7 (2013) 4733–4745, https://doi.org/10.1021/nn3036232.
[38] M. Jia, S. Li, L. Zang, X. Lu, H. Zhang, Analysis of biomolecules based on the surface enhanced raman spectroscopy, Nanomaterials 8 (2018).
[39] N.N. Durmanov, R.R. Guliev, A.V. Eremenko, I.A. Boginskaya, I.A. Ryzhikov, E. A. Trifonova, E.V. Putlyaev, A.N. Mukhin, S.L. Kalnov, M.V. Balandina, et al., Non-labeled selective virus detection with novel SERS-Active porous silver nanofilms fabricated by electron beam physical vapor deposition, Sens. Actuators. B Chem. 257 (2018) 37–47, https://doi.org/10.1016/j.snb.2017.10.022.
[40] X. Zhang, X. Zhang, C. Luo, Z. Liu, Y. Chen, S. Dong, C. Jiang, S. Yang, F. Wang, X. Xiao, Volume-enhanced raman scattering detection of viruses, Small. (2019) 15, https://doi.org/10.1002/smll.201805516.
[41] P. Negri, A. Kage, A. Nitsche, D. Naumann, R.A. Dluhy, Detection of viral nucleoprotein binding to anti-influenza aptamers via SERS, Chem. Commun. 47 (2011) 8635–8637, https://doi.org/10.1039/c0cc05433j.
[42] E.C. Dykeman, O.F. Sankey, Theory of the low frequency mechanical modes and Raman spectra of the M13 bacteriophage capsid with atomic detail, J. Phys. 21 (3) (2008 Dec 15) 035116.

[43] G.T. Hess, J.J. Cragnolini, M.W. Popp, M.A. Allen, S.K. Dougan, E. Spooner, H. L. Ploegh, A.M. Belcher, C.P. Guimaraes, M13 bacteriophage display framework that allows sortase-mediated modification of surface-accessible phage proteins, Bioconjug. Chem. 23 (2012) 1478–1487, https://doi.org/10.1021/bc300130z.

[44] J.A. Wood, B. Zhang, M.R. Tomkins, A. Docoslis, Numerical investigation of AC electrokinetic virus trapping inside high ionic strength media, Microfluid. Nanofluidics. 3 (2007) 547–560, https://doi.org/10.1007/s10404-006-0145-0.

[45] W.J. Chung, D.Y. Lee, S.Y. Yoo, Chemical modulation of m13 bacteriophage and its functional opportunities for nanomedicine, Int. J. Nanomedicine 9 (2014) 5825–5836, https://doi.org/10.2147/IJN.S73883.